Fatigue Crack Growth Behaviour in Friction Stir Welded Aluminium–Lithium Alloy Subjected to Biaxial Loads

Richter-Trummer, V. , Zhang, X. , Irving, P.E. , Pacchione, M. , Beltrão, M. and dos Santos, J.F.

Original citation:
Richter-Trummer, V. , Zhang, X. , Irving, P.E. , Pacchione, M. , Beltrão, M. and dos Santos, J.F. (2015) Fatigue Crack Growth Behaviour in Friction Stir Welded Aluminium–Lithium Alloy Subjected to Biaxial Loads. Experimental Techniques, volume In press. DOI: 10.1111/ext.12116

http://dx.doi.org/10.1111/ext.12116

Experimental Techniques (2015) ©2015, Society for Experimental Mechanics;
doi:10.1111/ext.12116

Fatigue crack growth behaviour in friction stir welded aluminium-lithium alloy subjected to biaxial loads

V. Richter-Trummer[1], X. Zhang[2], P. E. Irving[2], M. Pacchione[3],

M. Beltrão[4], J. F. dos Santos[4]

[1] *FEUP - Faculdade de Engenharia da Universidade do Porto,*

Rua Dr. Roberto Frias, 4200-465 Porto, Portugal

Valentin@fe.up.pt

[2] *Cranfield University, Bedfordshire MK43 0AL, United Kingdom*

[3] *Airbus Operations GmbH, Kreetslag 10, Hamburg, Germany*

[4] *Helmholtz-Zentrum Geesthacht , Institute of Materials Research,*

Materials mechanics, Solid-State Joining Processes,

Max-Planck-Straße 1, 21502 Geesthacht, Germany

January 26, 2016

Abstract

In the present paper, biaxial load fatigue crack growth tests are reported. Specimens were made of an advanced aluminium-lithium alloy AA2198-T8 joined by the friction stir welding process, capable of producing advanced integral metallic structures that can offer significant cost and weight savings over the current joining methods. Two material rolling directions are considered in relation to the

welding and crack growth direction. Welding-induced initial distortion was measured before the experiment for better result interpretation.

Test specimens are representative of two different weld orientations, i.e. longitudinal weld parallel to the material rolling direction and circumferential weld perpendicular to the material rolling direction for investigating the inherent material anisotropy of aluminium-lithium alloys. In all tests the fatigue crack was initiated in the thermo-mechanical process zone of the weld and propagated parallel to the weld joint line.

It is shown that the rolling direction of the selected aluminium alloy strongly affects the crack growth path. The specimens welded orthogonally to the rolling direction exhibit a shorter fatigue crack growth life than the specimens welded parallel to the rolling direction.

Keywords

AA2198, aluminium-lithium, biaxial, crack path, distortion, fatigue crack growth, FSW, testing setup

---

1 Introduction

Traditional aircraft structures have been assembled by riveting or bolting. This joining process leads to built-up structures, in which propagating cracks can be retarded or even arrested by intact structural members. Integral metallic structures, which may be fabricated by high speed machining or welding processes offer the benefit of reduced structural weight and reduced manufacturing cost; hence are very attractive. However, they inherently lack of fail-safety capability due to continuous crack growth path. Therefore their fatigue crack growth behaviour has to be thoroughly studied before this type of innovative design concept may be used in aircraft structures. Several studies

have been performed in this context, e.g. [1–5]. Most of the work published concerning fatigue crack propagation in lightweight structures, e.g. skin-stringer panels [5–7], have only considered the unidirectional load case. However, aircraft skin panels, especially the fuselage shells, are subjected to complex loads acting in two orthogonal directions.

Hannon and Tiernan have presented several approaches for biaxial testing systems and specimen designs, mostly for the static load experiments [8]. Most of these techniques may be adapted for fatigue tests. Test machine designs of different complexity have been developed, from the adaptation of uniaxial testing machines to tailor made multiaxial testing systems. Atkins et al. presented a special fixture that creates a biaxial stress field in cruciform specimens by using a standard uniaxial testing machine with different biaxiality ratios [9]. A similar approach was also used by Abu-Farha et al. [10] who studied various geometries for static biaxial load tests at elevated temperature. Biaxial fatigue resistance of polymeric plates was studied using a special fixture, which transforms the uniaxial compressive loads from a standard testing machine into biaxial tensile loads [11]. A similar system that adapts uniaxial testing machines for biaxial experiments was developed by Bhatnagar et al. [12]. This system is capable of applying any load relation between the two axes. It should be noted that with this kind of test setup the ratio between both axes is constant during the entire test, which may not be desirable. Therefore testing equipment with multiple and independently controlled loading devices can provide a more versatile setup. Some testing machines are commercially available and have been used successfully, e.g. for the thermoelastic approach for determining the stress intensity factor in a biaxial stress field [13], whereas some researchers used tailor made equipment [14]. In the present study the equipment was custom made by company Instron [15], and controlled by several interconnected servo-hydraulic controllers. Comparable systems with four independent actuators have already been used successfully before [16–18].

Specimen design is also challenging. Since no standard geometry exists yet, comparison of results

and extraction of data from different laboratories is difficult [8]. Dalle-Donne et al. have shown different biaxial specimen designs [19]. Smits et al. showed the advantages of using four actuators for cruciform specimens [20] and compared the geometries of small scale specimens made of composite material. They concluded that by reducing the thickness in the central gauge region and using a fillet between two adjacent arms, failure should be more likely to occur in the specimen centre region. While most of the cruciform specimens are made of thin sheets, Bass et al. showed a biaxial specimen with a thickness of over 100 mm for a research related to nuclear reactor pressure vessels [21]. Numerical models have been used to improve the specimen designs, e.g. [22–24].

Another challenge is the load transfer efficiency, so that applied load in one direction is transferred to the specimens centre gauge section as much as possible, generating minimum resistance in the perpendicular direction. The most commonly used cruciform specimens do have a square central gauge zone. To help the uniform load transfer (load diffusion), two types of specimens have been used. One type has reduced thickness in the central gauge section, and the other introduces a number of slots in the loading arms of the specimen [8, 25, 26]. A detailed study using photoelastic measurement was performed by Pisarenko et al. concerning the number of slots necessary for the load transfer [27]. They found that larger number of slots have resulted in much improved stress distribution in the specimen centre. Some researchers combine both types in their specimens [28, 29], as shown in Figure 1.

Design studies of the load-diffusion slots in the loading arms of cruciform specimens have been performed. For example, an odd number of slots is found to work better in reducing the local stresses [30]. A detailed finite element analysis (FEA) confirms that adding slots can improve the stress uniformity and increase the stress level closer to the intended loading level in the centre region [31]. This study also shows that the slots' width and number have significant influence, whereas the slots' length and location have little effect .

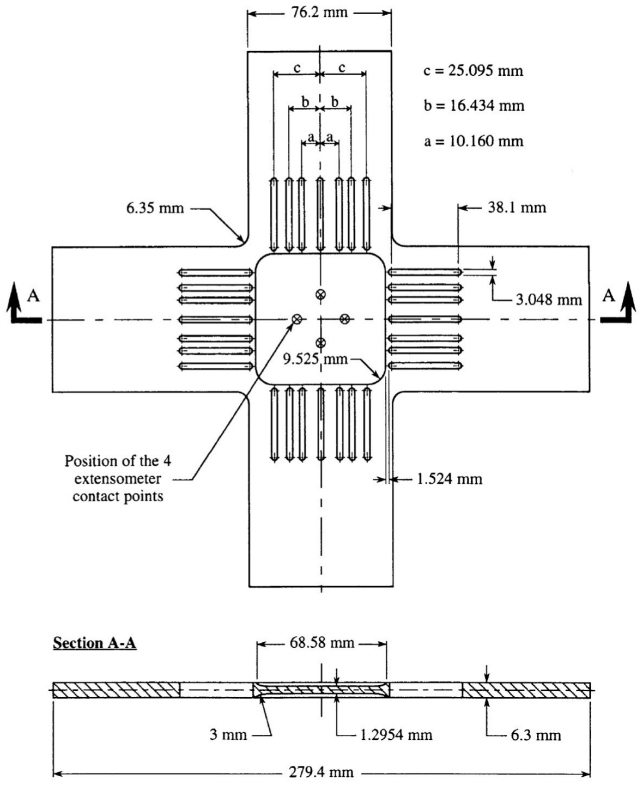

Figure 1: A cruciform specimen with reduced thickness in central test region and load diffusion slots [28]

The present work is also motivated by the increasing application of the third generation aluminium-lithium alloys in the aerospace industry and new joining technologies such as advanced solid state welding processes. Development in this front is partly driven by the demand in structure weight reduction and stiffness increase [32]. Up to its solubility limit of 4.2% [32], each weight percentage lithium reduces the aluminium alloy density by approximately 3% and increases its elastic modulus by 5% [33]. Precipitation hardening of aluminium lithium is achieved by artificial ageing after solution heat treatment [34].

Damage tolerant alloys, such as AA2198, have been developed for the commercial aircraft market that requires a combination of high specific strength, excellent damage tolerance and reduced weight [35]. Comparing to prior generations of Al-Li alloys, the lithium percentage in AA2198 is reduced, slightly reducing elastic modulus and increasing density, but the higher Cu concentration makes up for these losses contributing to a higher strength, thermal stability and toughness. Especially in the T8 heat-treatment condition good damage tolerance properties are found [35].

It should be noted that the alloy AA2198 is characterised by a relatively large anisotropy in mechanical and microstructural properties between the material rolling and the transversal directions. Cavaliere et al. studied the influence of this anisotropy on tensile and fatigue properties of 4 mm thick AA2198-T851 welded butt-joints. Longer fatigue life was found for base material loaded longitudinally to the rolling direction. However, this difference was not noticeable for the welded samples, probably due to the microstructural changes caused by the friction stir welding process [36, 37].

The friction stir welding (FSW) process was developed and patented by the TWI in 1991 [38] as a novel solid-state joining process with the ability to weld high strength aluminium alloys that are difficult to weld by fusion welding techniques. FSW can also join dissimilar materials [39].

Friction Stir Welding is a promising technique to solve the challenge of welding the AA2XXX series

high strength alloys, which were very difficult to weld by traditional welding processes [40]. FSW also has the ability to join different thicknesses and has other advantages like a low number of defects and lower distortion. Therefore it is already in use in the aerospace [41] and automotive industries for joining high strength aluminium alloys, providing clean and consistently high joint strengths.

This paper presents an investigation of fatigue crack propagation behaviour in a cruciform specimen subjected to a biaxial stress field. The specimen was made of an aerospace grade aluminium-lithium alloy AA2198-T8 joined by the FSW process.

2 Equipment

2.1 Test rig and setup for biaxial loading

Figure 2(a) shows the triaxial servo-hydraulic testing machine, which was originally developed by Schenck, later acquired by Instron Structural Testing Systems (IST). This triaxial testing machine is equipped with six 1 MN servo controlled hydraulic cylinders, which can be controlled simultaneously and independently. Only four of them were used in the modal control in the present work. This control scheme is a combination of force and displacement control, which guarantees the required load while maintaining the specimen centred in the loading rig. Figure 2 shows photographs of the setup that was used in this experiment. Figures 2(b) and 2(c) show the specimen being mounted inside the test rig unloaded when the zero level was set for strain measurement. The alignment of the specimen is guaranteed by a combination of the adjustable clamps mounted on the rigid cylinders and of the adopted clamping procedure aiming at reducing potential misalignments.

Parameters for the servo-hydraulic controller are listed in Table 1. Apart from the standard proportional (P), integral (I) and derivative (D) parts of the control algorithm a time delay (L) is

(a) Instron triaxial testing machine used in this study

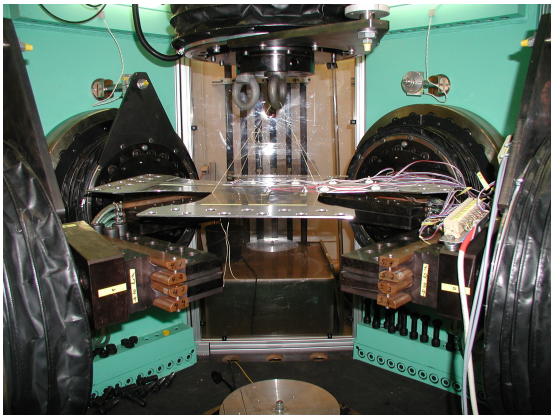

(b) Unclamped specimen at unloaded initial state (view a)

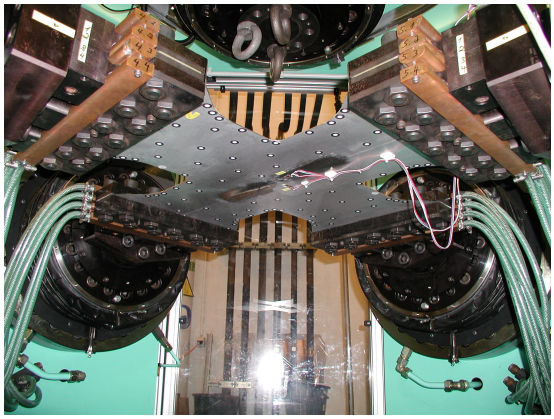

(c) Mounted specimen (view b)

Figure 2: Photos of the experimental setup

Table 1: PIDL values for the Instron servo-hydraulic modal controllers

	P [dB]	I [/s]	D [ms]	L [ms]
X-axis sum	4	0.6	0	75
Y-axis sum	4	0.6	0	0
X-axis difference	5	0.2	0	0
Y-axis difference	5	0.2	0	0

added in order to guarantee the required relation between all cylinders. Using the selected values, the required phase shift of 0° was achieved at a loading frequency of 4 Hz.

Before experiments were started, the uncertainty from the unloaded load cells was measured in order to gain insight into the best possible force control values. The maximum uncertainty from both axes obtained for all specimens with the hydraulic system turned off was determined to be 0.08 to 0.22 kN on the X-axis and 0.05 to 0.26 kN on the Y-axis for all specimens. No higher accuracy should be expected from this setup. It should be kept in mind that the load cells have a capacity of 1000 kN, which means that 0.1 kN is equivalent to a voltage drop of only 1 μV. This uncertainty was verified during the experiments and seemed not to influence the experiments. The uncertainty is influenced by various factors and cannot be controlled completely in such a complex setup.

Strain measurements were performed during the complete clamping process in order to guarantee that all information regarding each of the specimens is conveniently registered. The data were used to calibrate the numerical models, which do not simulate the initially distorted shape of the specimens due to the fabrication process.

2.2 Crack measurement device

Crack measurement was performed using an optical microscope, as shown in Figure 3. A charge coupled device (CCD) camera is connected to a Zeiss optical microscope with a Zeiss fibre optics light source. The crack tip was detected by the operator on a connected monitor. Prior experience of the author with automatically detected crack tips [42] lead to the decision to use manual crack tip detection in such a complex setup. This permits a good identification of the crack tip location. In order to define the crack tip position in the global coordinate system of the specimen, digital scales were attached to a table in the X and Y directions, see Figure 3(a). Using these scales the microscope can achieve accuracies better than 0.5mm, where the crack tip position was recorded with an accuracy of 0.1mm. Figure 3(b) shows the initial EDM notch of a specimen as an example. There was a further cut at the notch root by a very thin razor blade for easier fatigue crack initiation.

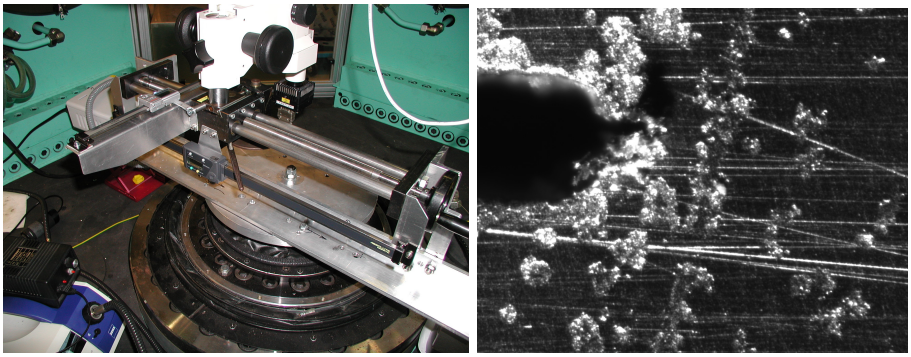

(a) Digital scales used for positioning the microscope exactly below the crack tip.

(b) Initial notch root as seen through the microscope.

Figure 3: Crack tip detection and crack length measurement.

3 Experimental setup and testing procedure

3.1 Specimen design

The cruciform specimen geometry was based on the review of some existing designs [8, 10, 20, 43]. In previous projects, a slot design in the loading arms was successfully used [43]. An example specimen for static tensile load test is shown in Figure 4. The radius of the fillet between two adjacent loading arms was 3 mm in this case.

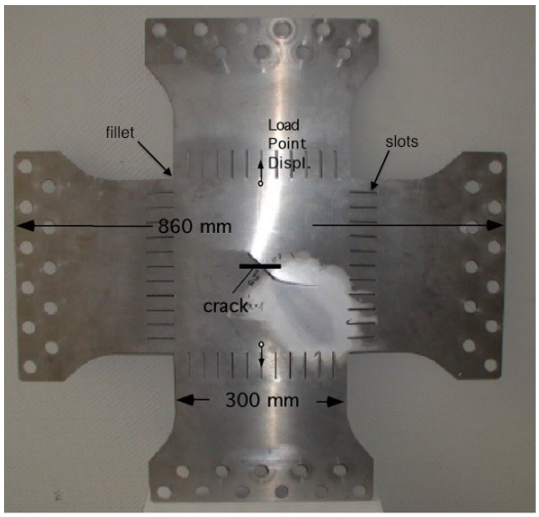

Figure 4: Photo of a HZG test sample for static tensile loading test with load-diffusion slots [43]

For the purpose of this study, i.e. testing under cyclic loads, the basic geometry shown in Figure 4 was revised based on the following concerns. First, for preventing cracks from initiating at the round fillets between two adjacent loading arms, the radius must be large enough to reduce the stress concentration effect. FEA (finite elements analysis) will also reveal whether enlarged radii will lead to the "cross-loading" effect between the loading arms. Second, since cyclic loads could cause fatigue failure at the small radius of the slots, these fatigue load specimens do not contain the load-diffusion slots.

Specimen design was based on FEA [31]. The numerical model has very fine mesh around the fillet curvature in order to capture the stress concentration accurately. Since cyclic loads could also cause fatigue failure at the small radius of the slots, test specimens planned for fatigue testing do not contain these slots. Selected fillet radii (r) were modelled. Calculated stress contour maps are shown in Figures 5 for r = 3 and 12 mm. It shows that the stress concentration factor (K_t) is significantly reduced with the higher radius. To minimise the risk of crack initiation from the corner fillet, r = 20 mm was selected for the final specimen design, where the K_t calculated by the finite element method is 3.2 [31].

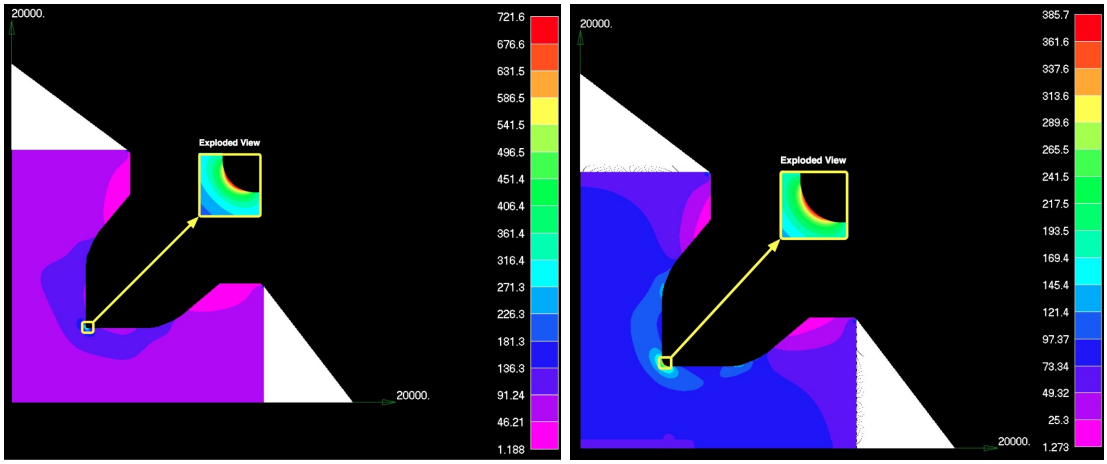

(a) Fillet radius 3 mm; K_t = 7.2

(b) Fillet radius 12 mm; K_t = 3.9

Figure 5: Von Mises stresses calculated by the finite element method for fillet radius (a) 3 mm and (b) 12 mm at applied biaxial stress of 100 MPa : 100 MPa. Stress concentration factor K_t = maximum von Mises stress / applied uniaxial stress in y-axis

Using the S-N curve of the AA2198-T8 aluminium alloy, the lower and upper bounds of fatigue crack initiation life were estimated at 1×10^6 to 6×10^6 cycles. This estimated fatigue life at a point located in the fillet is sufficiently longer than the cycle numbers required for fatigue crack propagation from a 40 mm pre-crack length to failure, which is the subject of this research. Fatigue

crack growth life was evaluated to be in the order of 10^5 [31]. Since the aim of the research reported in this and another related paper [44] is about crack propagation, radius r = 20 mm was chosen for the testing specimens.

Figure 6 shows a sketch of the specimens for a detailed coordinate system definition and the locations of strain gauges used for strain measurement on the two surfaces of the specimen. The notch is on the geometrical centre with the initial length of $2a_0$ = 40 mm. However, the weld is off-set from the centre in oder to set the crack on the welding retreating side, which is believed to have the poorest properties [3].

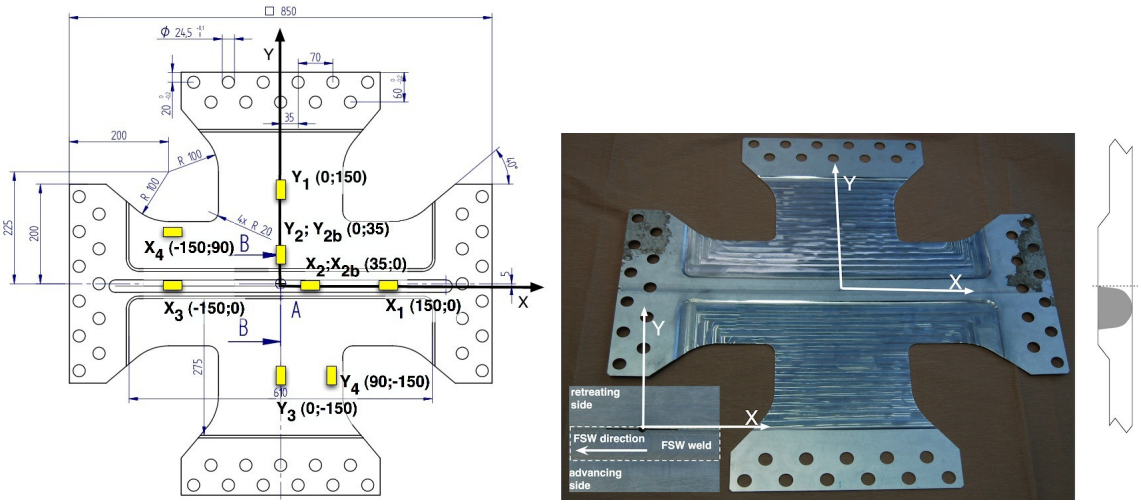

(a) engineering drawing (b) picture

Figure 6: Test specimen including the strain gauge positions. Note: gauges x_{2b} and y_{2b} are on the specimen back side

3.2 Material

Mechanical properties obtained from tensile tests on AA2198-T8 are available for the base material (BM) [45] and welded coupons (FSW) [46]. Bordesoules et al. have performed six tensile tests in the longitudinal direction and the average value was calculated [46]. Main properties are summarized

in Table 2, where various data sources are listed. Comparing to the base material properties, the welded joint has attained 63% of the yield strength and 94% of the elastic modulus.

Table 2: Mechanical properties for AA2198, both parent material and FSW

	base material measured by			FSW joint
	[45]	[35]	[36]	[46]
Young's modulus [GPa]	71		77	75
$\sigma_{y,0.2\%}[MPa]$	450	470	436	285
σ_{UTS} [MPa]	499	510	491	406
Elongation [%]	15	12	16	14

3.3 Welding process

Friction Stir Welding was performed using a MTS iStir 5 welding machine using the following welding parameters: downforce 8.5 kN, welding speed 500 mm/min, spindle rotation 1200 rpm and 0^o tilt angle. The tool used for welding had a scroll shoulder with a diameter of 13 mm and the pin was tapered from a diameter of 4.9 to 3.9 mm. The maximum pin length of 3 mm was adjusted automatically to have a distance of 0.2 mm from the backing bar.

All specimens, except the fourth, were made of rolled aluminium plates with a thickness of 3.2 mm. For the fourth specimen, a 4 mm thick plate was used, and after welding, the specimen was machined on the shoulder surface to the same thickness as the other three specimens. Two specimens (BIAX1, BIAX3) were welded orthogonally to the rolling direction, and another two (BIAX2, BIAX4) were welded parallel to the rolling direction. This was done to simulate both the transversal and longitudinal welds of a fuselage barrel.

3.4 Manufacturing induced distortion (and distortion control during testing)

A commercially available Pontos optical deformation measurement system from GOM mbH was used for measuring the initial shape of all specimens. The measurement system was used slightly outside of the recommended measurement volume due to the large specimen size, nevertheless a pixel deviation between 0.013 and 0.04 was found during calibration for the different specimens. In this context it should be noted that a value of up to 0.04 is acceptable for good measurement results according to the measurement system manufacturer. The uncertainty of the measurements was estimated to be below 0.1 mm. Furthermore, since all specimens were measured in the same conditions, comparability is guaranteed. Figure 7 shows the specimen BIAX3 being prepared for optical distortion measurement. The black and white markers used for the three-dimensional coordinate determination by the stereo vision based system are clearly visible.

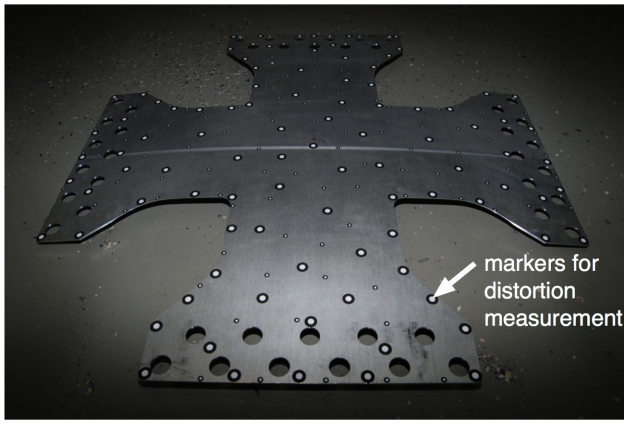

Figure 7: Specimen prepared for the out-of-plane distortion measurement by the optical system

The first of the analysed specimens was illuminated by a 2000 W halogen studio light. All subsequent specimens were illuminated by a LED based lighting system developed for such measurement tasks. This cold light source does provide a significantly friendlier working environment, without

Table 3: Measured overall distortion levels

Specimen	distortion [mm]	comment
BIAX1	24.9	rolling orthogonal to the weld
BIAX2	19.4	rolling parallel to the weld
BIAX3	25.0	rolling orthogonal to the weld
BIAX4	32.9	rolling parallel to the weld (was completely machined on the internal surface)

adversely affecting the measurement quality.

Schneider-Kreuznach lenses with a focal length of 50 mm and a maximum aperture of f/2.8 were used with an aperture of f/11 to guarantee a sharp image throughout the whole measurement volume.

The overall distortion was calculated by measuring the distance between two planes parallel to the least squares best fit plane through the centroid which englobe all measured points, see Table 3. In this way it is possible to compare complex shape distortions quantitatively with low effort. This information should however always be accompanied by a qualitative analysis of the measured shapes. It should be mentioned that the specimens own weight can influence the measured shape due to their small thickness, but in the current case all specimens were measured using the same setup, therefore the comparability between the specimens can be maintained.

Figure 8 shows the measured out-of-plane distortion of the specimens. The distorted shapes of the first three specimens (BIAX1, BIAX2, BIAX3) are almost identical, whereas BIAX4 differs by

bending in the opposite direction.

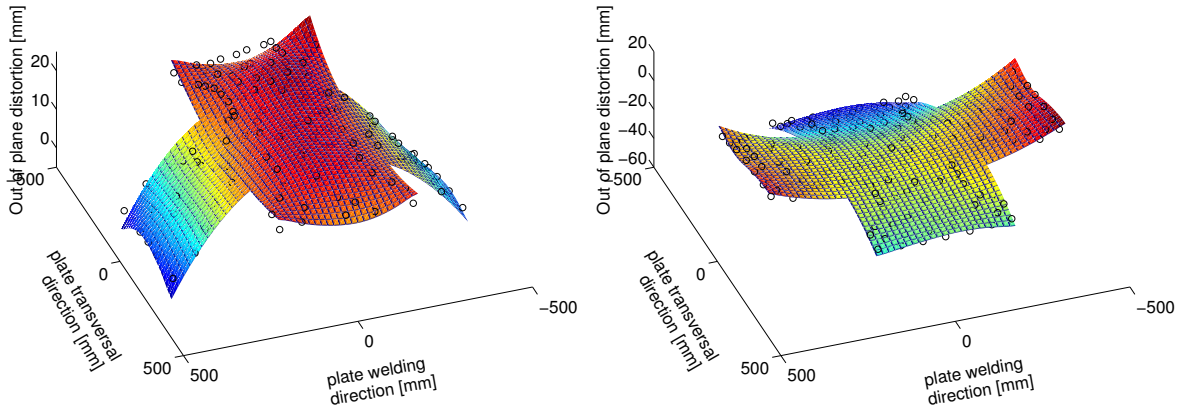

(a) Specimen BIAX3 (BIAX1 and BIAX2 had similar deformed shapes)

(b) Specimen BIAX4 (which was completely machined on the top surface to obtain the same material thickness as the other three specimens)

Figure 8: Measured out-of-plane distortion

Specimens welded orthogonally to the rolling direction (BIAX1, BIAX3) seemed to have a greater overall distortion after machining. It should be remembered that the specimen BIAX4 has a different shape distortion, which should not be considered for comparison. This is a result of milling the internal face of the plate in order to reduce its thickness of 4 mm to the same thickness of the other specimens before machining of the pockets, see Figure 8(b). It is most likely that this additional distortion is due to the redistribution of the residual stresses existing in the parent material when part of these residual stresses are relaxed [47].

The specimens were distorted due to the welding and machining processes, but were forced to an almost flat shape during clamping on the test machine. This means that, even before applying the external loads, initial strains are built up in the specimen, which are partially caused by the flattening forces acting on the distorted specimen. These initial strains may be significant if the initial distortion is significant, and should therefore be considered in numerical simulations. Table 4

Table 4: Clamping force induced initial strains (units: $\mu\varepsilon$)

Specimen	ε_{x1}	ε_{x2}	ε_{x3}	ε_{x4}	$\varepsilon_{x2\ ext.}$	ε_{y1}	ε_{y2}	ε_{y3}	ε_{y4}	$\varepsilon_{y2\ ext.}$
BIAX1	61	216	23	-172	101	609	476	596	270	-93
BIAX2	15	114	135	-171	95	540	446	489	343	-55
BIAX3	-49	-119	59	-338	-54	575	498	462	387	-182
BIAX4	147	-262	204	570	207	-209	-110	-161	-476	491

shows the measured strains due to the clamping force after reaching the load level of 4 kN (nominal zero load level before applying mechanical loads). Strain values of almost 600 $\mu\varepsilon$ are recorded on the specimen surface due to the initial distortion, and big differences among these specimens are found. In order to be able to compare the measured data with the numerical models that do not model the control of the initial distortion, after measuring the distortion-induced initial strains, all strain gauges were set to zero at the initial load of 4 kN.

3.5 Static load testing of the setup (and calibration)

Static load testing was performed in order to verify the numerical models, and to ensure that all specimens had similar initial conditions. Various load combinations between the X and Y axes were performed. In the first and second load scenarios (A, B), only the Y or X load axis was loaded up to the maximum load of 40 kN, leaving the other axis at the 4 kN minimum load. In the third test (C), both load axes were loaded up to the maximum fatigue load of 40 kN. In the forth test (D), only half of the maximum load was applied to the X axis, while the Y axis was fully loaded. Only the test D result is reported in this paper.

Different approaches have been used for measuring strains on biaxial specimens. Ramault et al. has compared electronic speckle pattern interferometry, digital image correlation (DIC) and the

traditional strain gauges [48]. DIC gives the most comprehensive information of the strain distribution on small specimens. In the current case, the larger specimen size and the difficulty to access it inside of the testing rig, have led to the use of strain gauges as a viable alternative. Since strain gauges are able to measure local strains very accurately only in one direction, the sensor locations shown in Figure 6 were chosen in order to acquire the required distribution for the present case. HBM strain gauges with a nominal resistance of 350 Ω and a gauge length of 3 and 6 mm were used.

Before the static loading experiment, the specimens were loaded up to 10 kN three times and afterwards the strain gauges were set to zero at a load of 4 kN. At this load the specimens were flat inside the testing rig.

Strain distribution versus the applied load is shown in Figure 9 for the first specimen. The Y axis was loaded up to the maximum load of 40 kN in 5 kN incremental steps, and the X axis was simultaneously loaded up to 50% of the maximum load in the same incremental steps.

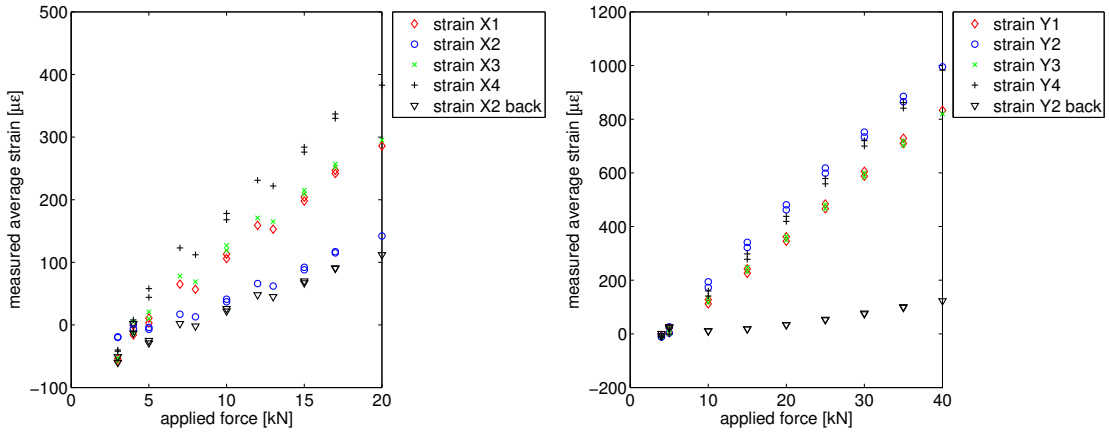

(a) X axis

(b) Y axis

Figure 9: Strain distribution with applied load (specimen BIAX1, load scenario D)

Strain readings were linear with the increasing load, further validating the clamping setup and

general quality of the testing setup. The strain in X direction begins at negative values, since the strain gauges were balanced at a load of 4 kN, but loading scenario "D" includes lower values in X direction. This static loading data were used to validate the finite element model which is reported in a separate paper [44]. Additionally this measured data demonstrated that all specimens were tested under the same loading conditions and that the clamping of each of the specimens has lead to similar initial load levels in the specimens. The stress in the central testing area was shown to be uniform and represents the required stress biaxiality.

3.6 Fatigue loading scenario

Due to manufacturing considerations, aluminium panels are much longer in the rolling direction than in the transverse direction. Fuselage panels are manufactured, with very few exceptions, with the rolling direction oriented in the aircraft flight direction, since in this way longer panels can be produced and the number of circumferential joints can be reduced.

Therefore specimens welded orthogonally to the rolling direction mimic the circumferential joints, whereas specimens welded parallel to the rolling direction simulate the longitudinal joints. Load ratio 1:1 represents the upper fuselage panel under the bending and cabin pressurisation loads. The maximum applied stress of 100 MPa was defined for research. It was chosen to test the effect of initial cracks in the thermo mechanical process zone of the welds in joint direction, since this had previously been considered the most relevant situation.

Therefore the fatigue load was defined by sinusoidal loads with a maximum load of 40 kN (corresponding to 100 MPa) and minimum load of 4 kN (at load ratio R = 0.1). The loading in both directions, X and Y, was applied without phase-shift.

4 Results

4.1 Fatigue crack growth life

Figure 10 shows the test measured crack length vs. numbers of cycles of all specimens. All crack length measurements were taken with the maximum load of 40 kN applied to the Y-axis and the minimum load of 4 kN applied to the X-axis. In order to be able to compare the results more accurately, the results are plotted for a initial notch $a_0 = 21mm$, which means that the initial load cycles for developing a crack from the notch root to the initial crack size were not considered. Note "a" is half crack length.

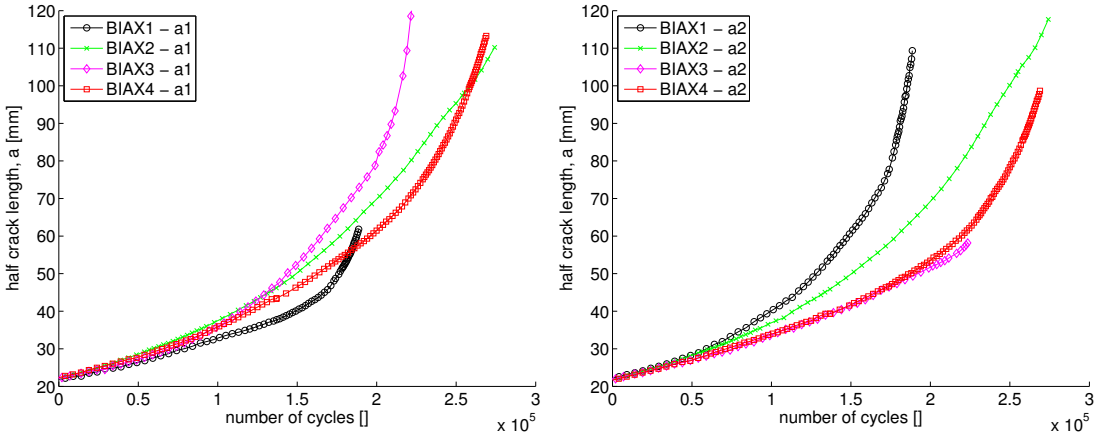

(a) Crack on the left hand side (a_1)

(b) Crack on the right hand side (a_2)

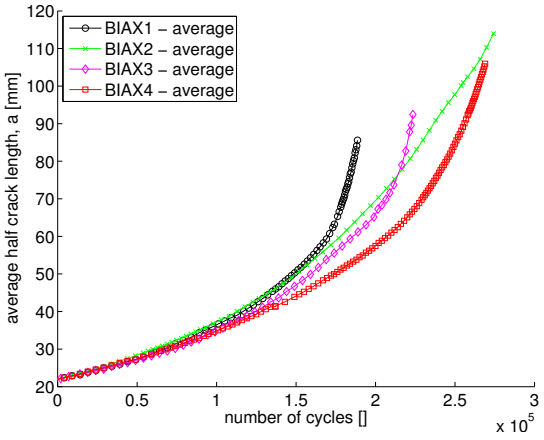

(c) Average half crack length (a_{av})

Figure 10: Crack growth lives for all four specimens

4.2 Crack growth path

Figure 11 and 12 show test measured crack growth trajectories. The initial notch ($2a_0$) as shown in Figure 11 was aligned orthogonally to the rolling direction, placed in the weld transition zone at the retreating side. It can be seen that the crack propagation had significantly deviated from the centre line. Crack growth was not symmetric about the notch. In contrast to this behaviour, cracks shown in Figure 12 grew symmetrically and also well aligned with the initial notch. In these specimens (BIAX2, BIAX4), the initial notch was also parallel to the material rolling direction.
The difference between the results of a crack growing either in parallel or perpendicular directions to the material rolling directions is apparent. Specimens welded orthogonally to the rolling direction had asymmetrical fatigue crack growth behaviour compared to the specimens welded parallel to this direction.

5 Discussion

Figure 11 clearly shows that the crack growth rate was slower on the side where the crack tip entered the welded material and propagated towards the weld nugget, which was also reported by Richter-Trummer et al. for other materials [2], and also partially observed in the same alloy AA2198 by uniaxial load tests [3, 49, 50]. In this case, residual stress arising from the welding process may have affected the results. Since the simpler specimen is comparable to the cruciform specimens tested in the present work in terms of the welding orientation and crack path in the weld, similar crack growth behaviour may be expected.
Figure 13 shows fatigue crack growth rates in M(T) specimens that were also made of the AA2198 alloy; both parent material and welded butt joint that is perpendicular to the load direction. It shows that crack growth rates in the weld nugget are slower than that in the parent material.

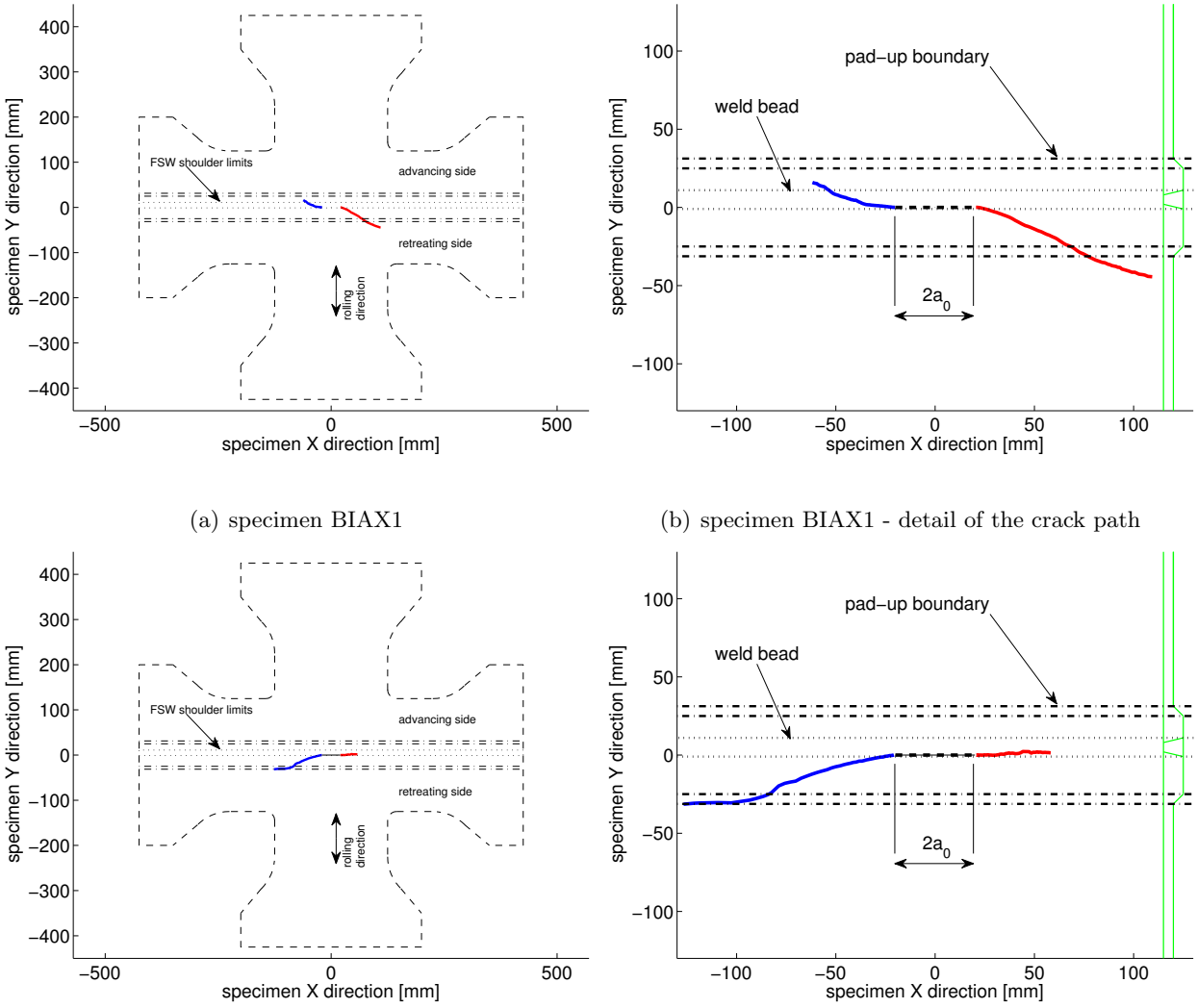

(a) specimen BIAX1

(b) specimen BIAX1 - detail of the crack path

(c) specimen BIAX3

(d) specimen BIAX3 - detail of the crack path

Figure 11: Measured crack growth trajectories in specimens with welding pass orthogonal to the rolling direction

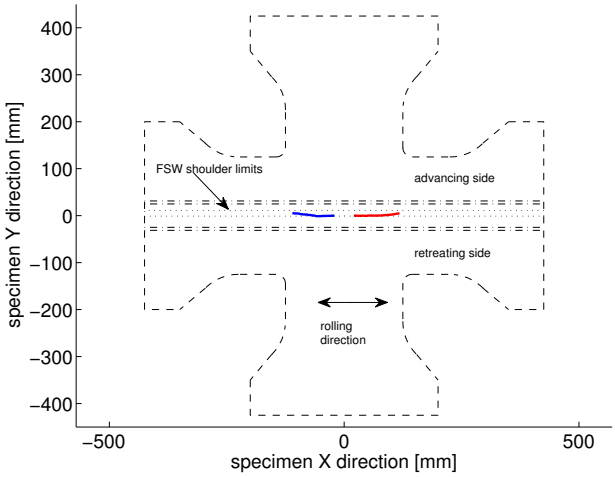

(a) specimen BIAX2

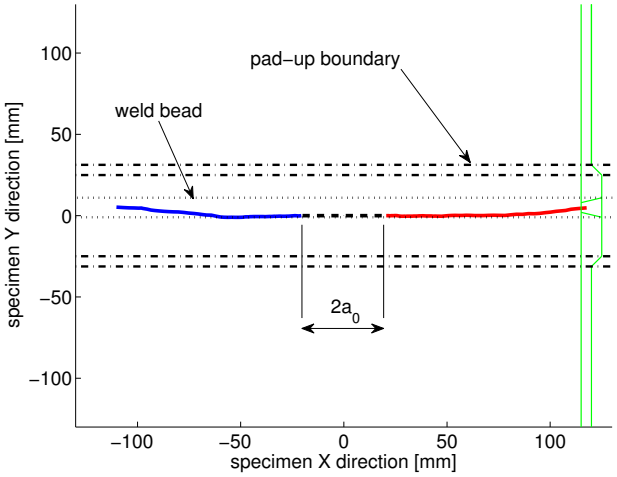

(b) specimen BIAX2 - detail of the crack path

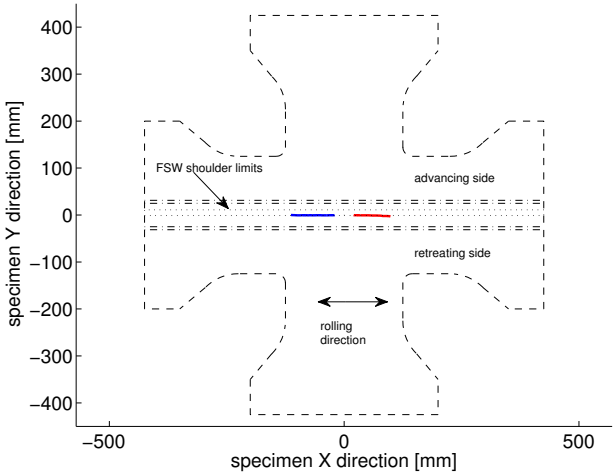

(c) specimen BIAX4

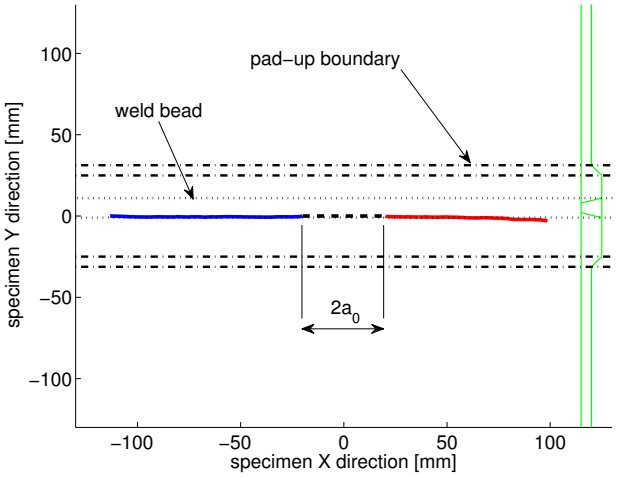

(d) specimen BIAX4 - detail of the crack path

Figure 12: Measured crack growth trajectories in specimens with welding pass parallel to the rolling direction

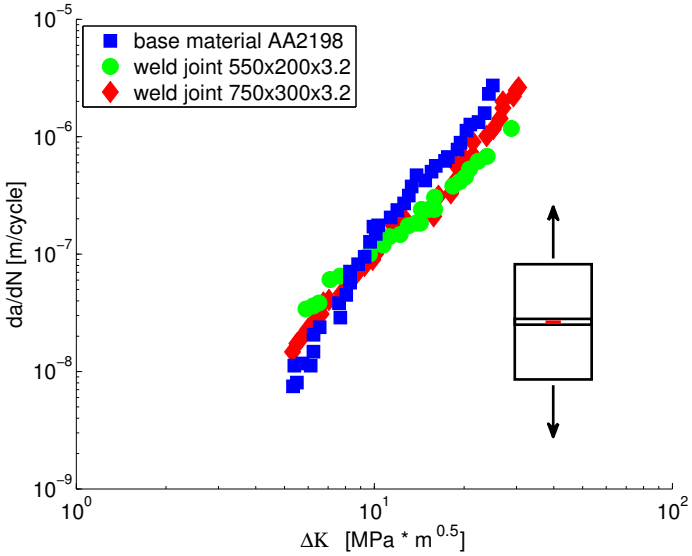

Figure 13: Fatigue crack growth rates comparison between welded and base material [49]

This result helps to explain the lower crack growth rate on the side that the crack has entered the weld zone. However, these M(T) specimen test results do not explain the difference in crack trajectory that is related to the material rolling direction. Material inherent anisotropy may be a factor. In this research, just one crack scenario was chosen, having the crack initiating in the thermo-mechanical affected zone (TMAZ) and propagating parallel to the weld. Another scenario is having a crack propagating perpendicular to the weld, which was not studied in this work.

6 Conclusions

Fatigue crack growth tests under biaxial loads have been performed for cruciform specimens made of Al-Li alloy AA2198-T851 containing a butt joint fabricated by the friction stir welding process. The initial notch location was in the thermo-mechanical affected zone on the retreating side of the friction stir weld. Biaxial load ratio was kept at 1:1. Following conclusions can be drawn:

1. Test setup and experimental procedures developed in this research are suitable for testing

thin-walled cruciform specimens.

2. Fatigue crack has a tendency of resisting entering the weld material and the preferred crack growth path in the present case was the material rolling direction; consequently, crack growth behaviour is different in specimens with weld parallel or transversal to the rolling direction.

3. Crack growth path was symmetric in the specimens with weld parallel to the material rolling direction.

4. Specimens welded orthogonally to the material rolling direction, with the crack growing parallel to the weld, exhibited a shorter fatigue life than specimens welded parallel to the rolling direction.

Acknowledgements

The authors acknowledge the work of J. Knaack, A. Roos, K.-H. Balzereit and O. Kreinbring. The present work was partially funded by the European Union COINS project and the PhD scholarship SFRH/BD/41061/2007 of the Portuguese Fundação para a Ciência e Tecnologia.

References

[1] R. G. Pettit, J. J. Wang, C. Toh. *Validated feasibility study of integrally stiffened metallic fuselage panels for reducing manufacturing costs.* NASA/CR-2000-209342 (May 2000).

[2] V. Richter-Trummer, S. M. O. Tavares, P. M. G. P. Moreira, P. M. S. T. de Castro. *Friction stir welding of aluminium alloys and damage tolerance of integral monolithic structures.* Mechanika, **73**(5):pp. 18–22 (2008).

[3] M. Pacchione, S. Werner, N. Ohrloff. *Design principles for damage tolerant butt welded joints*

for application in the pressurized fuselage. In: L. Lazzeri, A. Salvetti (eds.), *ICAF 2007, durability and damage tolerance of aircraft structures: metals and composites, proceedings of the 24th symposium of the ICAF, Naples*, pp. 224–240. Pacini, Pisa (2007).

[4] I. Scheider, W. Brocks. *Residual strength prediction of a complex structure using crack extension analyses.* Engineering Fracture Mechanics, **76**(1):pp. 149–163 (Jan 2009). doi: 10.1016/j.engfracmech.2008.06.035.

[5] M. V. Uz, M. Kocak, F. Lemaitre, J.-C. Ehrstroem, S. Kempa, F. Bron. *Improvement of damage tolerance of laser beam welded stiffened panels for airframes via local engineering.* International Journal of Fatigue, **31**(5):pp. 916–926 (MAY 2009). doi:10.1016/j.ijfatigue.2008.10.003.

[6] P. M. G. P. Moreira, V. Richter-Trummer, S. M. O. Tavares, P. M. S. T. de Castro. *Characterization of fatigue crack growth rate of AA6056 T651 and T6: Application to prediction of fatigue behaviour of stiffened panels.* Material Science Forum, **636-637**:pp. 1511–1517 (January 2010).

[7] S. M. O. Tavares, V. Richter-Trummer, P. M. G. P. Moreira, P. M. S. T. de Castro. *Fatigue crack growth modeling in stiffened panels considering residual stress effects.* Materials Science Forum, **636-637**:pp. 1172–1177 (2010).

[8] A. Hannon, P. Tiernan. *A review of planar biaxial tensile test systems for sheet metal.* Journal of Materials Processing Technology, **198**(1-3):pp. 1–13 (Mar 2008). doi: 10.1016/j.jmatprotec.2007.10.015.

[9] A. Atkins, G. Jeronimidis, S. Arndt. *Biaxial monotonic and fatigue fracture of some commercial ABS and PVC sheets.* Journal of Materials Science, **33**(17):pp. 4349–4356 (Sep 1998).

[10] F. Abu-Farha, J. Hector, L. G., M. Khraisheh. *Cruciform-shaped specimens for elevated temperature biaxial testing of lightweight materials.* Jom, **61**(8):pp. 48–56 (Aug 2009).

[11] H. Kwon, P. Jar, Z. Xia. *Characterization of bi-axial fatigue resistance of polymer plates.* Journal of Materials Science, **40**(4):pp. 965–972 (Feb 2005).

[12] N. Bhatnagar, R. Bhardwaj, P. Selvakumar, M. Brieu. *Development of a biaxial tensile test fixture for reinforced thermoplastic composites.* Polymer Testing, **26**(2):pp. 154–161 (Apr 2007). doi:10.1016/j.polymertesting.2006.09.007.

[13] R. Tomlinson, L. Marsavina. *Thermoelastic investigations for fatigue life assessment.* Experimental Mechanics, **44**(5):pp. 487–494 (Oct 2004). doi:10.1177/0014485104046091.

[14] X. Wu, M. Wan, X. Zhou. *Biaxial tensile testing of cruciform specimen under complex loading.* Journal of Materials Processing Technology, **168**(1):pp. 181–183 (Sep 2005). doi:10.1016/j.jmatprotec.2004.11.003.

[15] *www.instron.com* (July 2010).
URL `www.instron.com`

[16] K. J. Pascoe, J. W. R. de Villiers. *Low cycle fatigue of steels under biaxial straining.* The Journal of Strain Analysis for Engineering Design, **2**(2):pp. 117–126 (1967).

[17] T. Itoh, M. Sakane, M. Ohnami. *High temperature multiaxial low cycle fatigue of cruciform specimen.* Journal of Engineering Materials and Technology, **116**:pp. 90–98 (1994).

[18] M. Poncelet, G. Barbier, B. Raka, S. Courtin, R. Desmorat, J. C. Le-Roux, L. Vincent. *Biaxial high cycle fatigue of a type 304l stainless steel: Cyclic strains and crack initiation detection by digital image correlation.* European Journal of Mechanics A/Solids, **29**:pp. 810–825 (2010).

[19] C. Dalle Donne, K.-H. Trautman, H. Amstutz. *Multiaxial Fatigue and Deformation: Testing and Prediction*, chap. Cruciform Specimens for In-Plane Biaxial Fracture, Deformation, and Fatigue Testing, pp. 405–422. ASTM STP 1387. American Society for Testing and Materials, West Conshohocken, PA (2000).

[20] A. Smits, D. Van Hemelrijck, T. Philippidis, A. Cardon. *Design of a cruciform specimen for biaxial testing of fibre reinforced composite laminates.* Composites Science and Technology, **66**(7-8):pp. 964–975 (Jun 2006). doi:10.1016/j.compscitech.2005.08.011.

[21] B. Bass, W. McAfee, P. Williams, W. Pennell. *Fracture assessment of shallow-flaw cruciform beams tested under uniaxial and biaxial loading conditions.* Nuclear Engineering and Design, **188**(3):pp. 259–288 (May 1999).

[22] E. Lamkanfi, W. Van Paepegem, J. Degrieck, C. Ramault, A. Makris, D. Van Hemelrijck. *Strain distribution in cruciform specimens subjected to biaxial loading conditions. part 1: Two-dimensional versus three-dimensional finite element model.* Polymer Testing, **29**(1):pp. 7–13 (Feb 2010). doi:10.1016/j.polymertesting.2009.08.009.

[23] I. H. Wilson, D. J. White. *Cruciform specimens for biaxial fatigue tests: An investigation using finite-element analysis and photoelastic-coating techniques.* The Journal of Strain Analysis for Engineering Design, **6**(1):pp. 27–37 (1971). doi:10.1243/03093247V061027.

[24] A. Makris, T. Vandenbergh, C. Ramault, D. Van Hemelrijck, E. Lamkanfi, W. Van Paepegem. *Shape optimisation of a biaxially loaded cruciform specimen.* Polymer Testing, **29**(2):pp. 216–223 (Apr 2010). doi:10.1016/j.polymertesting.2009.11.004.

[25] D. R. Hayhurst. *A biaxial-tension creep-rupture testing machine.* The Journal of Strain Analysis for Engineering Design, **8**(2):pp. 119–123 (1973). doi:10.1243/03093247V082119.

[26] J. C. Morisson. *Techniques for Multiaxial Creep testing*, chap. Biaxial testing cruciform specimens, pp. 111–126. Elsevier Applied Science (1985).

[27] G. S. Pisarenko, V. P. Naumenko, E. E. Onishchenko. *A method of investigating the fracture of sheet materials in biaxial loading.* Strength of Materials, **14**(3):pp. 275–282 (1982). doi: 10.1007/BF00776036.

[28] D. E. Green, K. W. Neale, S. R. MacEwen, A. Makinde, R. Perrin. *Experimental investigation of the biaxial behaviour of aluminium sheet.* International Journal of Plasticity, **20**(8-9):pp. 1677–1706 (2004).

[29] W. M. Johnston, W. D. Pollock, D. S. Dawicke. *Biaxial testing of 2195 aluminum alloy using cruciform specimens.* techreport NASA/CR-2002-211942, NASA (2002).

[30] S. Demmerle, J. P. Boehler. *Optimal design of biaxial tensile cruciform specimens.* Journal of the Mechnics and Physics of Solids, **41**(1):pp. 143–181 (1993).

[31] H. Zhang. *Numerical Modelling of Crack Propagation in a Friction Stir Welded Cruciform Specimen.* MSc thesis, Cranfield University (2010).

[32] E. J. Lavernia, T. S. Scrivatsan, F. A. Mohamed. *Review strength, deformation, fracture behaviour and ductility of aluminium-lithium alloys.* Journal of Materials Science, **25**:pp. 1137–1158 (1990).

[33] M. Knüwer, J. Schumacher, H. Ribes, F. Eberl, B. Bes. *2198 - Advanced Aluminium-Lithium alloy for A350 skin sheet application.* In: *Aeromat Conf.* (May 2006).

[34] E. Starke, T. Sanders, I. Palmer. *New approaches to alloy development in the Al-Li system.* Journal of Metals, **33**(8):pp. 24–33 (1981).

[35] T. Warner. *Recently-developed aluminium solutions for aerospace applications.* Aluminium Alloys 2006, Pts 1 and 2, **519-521**:pp. 1271–1278 (2006).

[36] P. Cavaliere, A. de Santis, F. Panella, A. Squillace. *Effect of anisotropy on fatigue properties of 2198 Al-Li plates joined by friction stir welding.* Engineering Failure Analysis, **16**(6):pp. 1856–1865 (Sep 2009). doi:10.1016/j.engfailanal.2008.09.024.

[37] P. Cavaliere, M. Cabibbo, F. Panella, A. Squillace. *2198 Al-Li plates joined by friction stir welding: Mechanical and microstructural behavior.* Materials & Design, **30**(9):pp. 3622–3631 (Oct 2009). doi:10.1016/j.matdes.2009.02.021.

[38] TWI. *FSW* (2010).
URL `http://www.twi.co.uk/content/fswintro.html`

[39] P. M. G. P. Moreira, T. dos Santos, S. M. O. Tavares, V. Richter-Trummer, P. Vilaça, P. M. S. T. de Castro. *Mechanical characterization of friction stir welds of two dissimilar aluminium alloys of the 6xxx series.* Advanced Materials Forum IV, **587-588**:pp. 430–434 (2008). (paper presented at the 13th Conference of the Sociedade Portuguesa de Materiais/4th International Materials Symposium, Apr 1-4, 2007 Porto, Portugal).

[40] R. A. Cobden. *Aluminium: Physical Properties, Characteristics and Alloys.* No. 1501 in TALAT Lecture. Banbury (1994).

[41] *Eclipse aerospace* (September 2010).
URL `http://www.eclipseaviation.com/`

[42] V. Richter-Trummer, E. A. Marques, F. J. P. Chaves, J. M. R. S. Tavares, L. F. M. da Silva, P. M. S. T. de Castro. *Analysis of crack growth behavior in a double cantilever beam adhesive*

fracture test by different digital image processing techniques. Mat.-wiss. u. Werkstofftech., **42**(5):pp. 452–459 (2011). doi:10.1002/mawe.201100807.

[43] J. Heerens, M. Schoedel. *Characterization of stable crack extension in aluminium sheet material using the crack tip opening angle determined optically and by the δ_5 clip gauge technique.* Engineering Fracture Mechanics, **76**(1):pp. 101–113 (January 2009). doi: 10.1016/j.engfracmech.2008.04.009.

[44] X. Zhang, H. Zhang, R. Bao. *Predicting mode-I fatigue crack growth behaviour in a welded cruciform joint under biaxial stresses.* In: *Int Congress of Fracture (ICF13).* Beijing (16-21 June 2013).

[45] A. Ferreri. *Influence of thickness difference in friction stir welding of tailor welded blanks.* Master's thesis, GKSS (July 2009).

[46] I. Bordesoules, S. Gourdet, F. Marie, G. Moore, S. Morgan, A. Prisco, J. F. dos Santos, J. Silvanus. *Test data on new similar and dissimilar alloys.* COINS deliverable D4.2 (April 2010).

[47] V. Richter-Trummer, D. Koch, A. Witte, J. F. dos Santos, P. M. S. T. de Castro. *Methodology for prediction of distortion of workpieces manufactured by high speed machining based on an accurate through-the-thickness residual stress determination.* The International Journal of Advanced Manufacturing Technology, **68**(9):pp. 2271–2281 (2013).

[48] C. Ramault, A. Makris, D. Van Hemelrijck, E. Lamkanfi, W. Van Paepegem. *Comparison of different techniques for strain monitoring of a biaxially loaded cruciform specimen.* Strain, (in press) (June 2010). doi:10.1111/j.1475-1305.2010.00760.x.

[49] P. E. Irving, Y. E. Ma, X. Zhang, G. Servetti, G. Lampeas, I. Diamantakos, F. Marie, D. De-

loison, A. Sollo, S. Morgan, L. Rossi, A. Prisco, E. Gratiot. *Design considerations for integral structure including the effects of residual stress and cracks.* Report Nr. D15, COINS; FP6-2005-Aero-1; Contract No. AST5-CT-030825 (March 2010).

[50] P. E. Irving, Y. E. Ma, X. Zhang, G. Servetti, S. Williams, G. Moore, J. dos Santos, M. Pacchione. *Control of crack growth rates and crack trajectories for enhanced fail safety and damage tolerance in welded aircraft structures.* In: *25th ICAF Symposium.* Rotterdam (May, 27-29 2009).